Results in Chemistry 28 (2026) 103620

Contents lists available at ScienceDirect

Results in Chemistry

journal homepage: www.sciencedirect.com/journal/results-in-chemistry

"Mechanochemical synthesis and spectroscopic analysis of Cu^{2+} loading in ZIF-62"

Marija Švegovec [a,b], Andraž Krajnc [a], Ksenija Maver [b], Nataša Zabukovec Logar [a,b,*]

[a] National Institute of Chemistry, Hajdrihova 19, SI-1001 Ljubljana, Slovenia
[b] University of Nova Gorica, Vipavska 13, SI-5000 Nova Gorica, Slovenia

ARTICLE INFO

Keywords:
Zeolitic imidazolate frameworks
ZIF-62
Copper doping
Mechanochemistry
Glass formation

ABSTRACT

Metal organic frameworks (MOFs) provide customisable structures for gas separation, catalysis, and glass production. Among them, zeolitic imidazolate frameworks (ZIFs) stand out for their thermal stability and ability to yield melt-quenched glasses. ZIF-62, a well-studied glass-forming MOF, exhibits limited compositional flexibility, particularly when attempts are made to introduce transition metals. This study explores copper incorporation into ZIF-62 via mechanochemical and solvothermal synthesis. X-ray diffraction indicated ZIF-62 framework formation when acetate was used as a copper source by mechanochemical synthesis; however, complementary spectroscopic techniques (XAS, solid-state NMR, FTIR, Raman, DR UV-VIS, ICP-OES) showed that copper was not integrated into the framework. Instead, Cu species preferentially adopted coordination environments incompatible with the Zn-imidazolate framework structure and were more likely associated with surface or pore environments. Thermal analysis revealed reduced melting and glass transition temperatures in Cu-containing samples, demonstrating that even non-framework Cu species can influence the thermal behaviour of ZIF-62. Additional solvothermal synthesis attempts involving several Cu-containing precursors yielded crystalline or amorphous phases distinct from ZIF-62, further highlighting the strong influence of Cu coordination chemistry on framework formation. These findings demonstrate that Cu incorporation into ZIF-62 is strongly limited under the mechanochemical and solvothermal conditions explored in this work, emphasizing the importance of precursor selection and metal–ligand coordination preferences in the design of mixed-metal MOFs.

1. Introduction

Metal-organic frameworks (MOFs) are a type of hybrid material made up of inorganic nodes or clusters that are linked together by organic ligands. [1] Their one-of-a-kind designs, which mix adjustable porosity with tunable functionality, make them useful for many applications, including drug delivery, gas storage and separation, catalysis, and energy storage. [2–10] Zeolitic imidazolate frameworks (ZIFs), a sub-group of MOFs and topologically comparable to zeolites, exhibit stability at high temperatures and in different chemicals, which makes them very attractive for large scale use as adsorbents [11–15] or catalysts [16–18]. Two ZIFs in particular, ZIF-4 ($Zn(Im)_2$) and ZIF-62 ($Zn(Im)_{1.75}(bIm)_{0.25}$), featuring zinc-based nodes and imidazolate-derived linkers are widely studied. What sets these materials apart is their ability to melt and form glassy, amorphous phases upon quenching, a rare property among MOFs. [19–21] Their thermal behaviour is highly sensitive to both metal and ligand types, making them ideal platforms for studying compositional effects on framework properties. [22–25] One particularly effective strategy for tuning their behaviour, without altering the underlying topology, is mixed-metal approach. Incorporation of transition metals such as Co^{2+}, Ni^{2+}, Fe^{2+}, Cd^{2+}, and Mn^{2+} has been shown to impact gas sorption, optical properties, and structural or thermal stability. [23,26–30]

Copper is well-known for its function in redox chemistry and catalysis. [31–34] However, its incorporation into glass-forming ZIFs such as ZIF-4 and ZIF-62 has received relatively little attention. Although there have been reports of numerous copper-imidazolate frameworks, they usually create different topologies than those forming MOF glasses. The first example, $Cu(Im)_2$ with a *pts* topology, was synthesized by Jarvis and Wells in 1960 [35], laying the foundation for copper MOF chemistry. Later, Henke et al. [36] built on this work by looking at how copper–imidazolate systems melt and create glass. Recent work [17] has shown that Cu^{2+} doping into ZIF-8 works well, with $Zn_{1-x}Cu_x$-ZIF-8 compositions ranging from x = 0.1 to 0.25, and amorphous products

* Corresponding author at: National Institute of Chemistry, Hajdrihova 19, SI-1001 Ljubljana, Slovenia.
E-mail address: natasa.zabukovec@ki.si (N.Z. Logar).

https://doi.org/10.1016/j.rechem.2026.103620
Received 25 March 2026; Accepted 6 July 2026
Available online 7 July 2026

observed at higher copper loadings (x = 0.5). Increased copper content was found to reduce nucleation rates, leading to larger particle sizes.

Importantly, because Cu^{2+} and Zn^{2+} have comparable ionic radii (0.71 Å and 0.74 Å, respectively), copper incorporation did not significantly distort the framework, suggesting that copper may be introduced as a second metal node without disrupting the structure. [17] Nevertheless, Cu^{2+} (d^9) complexes are much more adaptable, taking on 4-, 5-, or 6-coordinate geometries based on the ligand environment [37], whereas Zn^{2+} in ZIFs is usually limited to tetrahedral coordination. This broader coordination flexibility, often driven by the Jahn–Teller effect and ligand field stabilization energy [38], is an important factor when interpreting how Cu distributes within the mixed-metal ZIF-62 framework. ZIFs are most commonly synthesized through solvothermal methods, where metal salts and imidazolate-based linkers react in solvents such as *N*,*N*-dimethylformamide (DMF). Although effective, these reactions typically require long durations, high temperatures, and large excesses of linker, resulting in considerable waste and limited scalability. [3,39,40] By contrast, mechanochemical synthesis, including solvent-free or liquid-assisted grinding, offers a faster and more environmentally friendly alternative. It enables improved stoichiometric control, fewer side products, and has been widely adopted for ZIF formation. [41,42] Notably, it has been used to prepare ZIF-62 and its mixed-metal analogues (Co/Zn) at gram scale, allowing tight control over metal and linker composition. [23]

In this study, we investigate the structural incorporation of Cu^{2+} into the ZIF-62 framework, with particular interest in how copper affects the local environment and the overall integrity of the structure. We explored both solvothermal and mechanochemical synthesis routes; however, only mechanochemistry led to the formation of ZIF-62-type materials in the presence of copper, prompting a more detailed structural analysis. To determine the extent and nature of copper incorporation, we employed a suite of techniques including X-ray absorption spectroscopy (XAS), solid-state NMR, FTIR, Raman spectroscopy, and ICP-OES. The influence of structural changes introduced through Cu^{2+} on ZIF-62's thermal behaviour and possible glass fabrication is also briefly discussed.

2. Experimental

2.1. Materials

Imidazole (99%), benzimidazole (98%) and ZnO (<100 nm) were purchased from Aldrich, $Cu(OAc)_2{\cdot}H_2O$ (98%), $Cu(NO_3)_2{\cdot}3H_2O$ (99%), gamma-valerolactone (GVL) (99%) and 1-Butanol were purchased from Sigma Aldrich. $CuSO_4{\cdot}5H_2O$ (99.5%) was purchased from Carlo Erba. Ethanol was purchased from Stella TECH. Methanol was purchased from Honeywell Riedel-de Haen. All materials were used without further purification.

2.2. Mechanochemical synthesis

All of the reagents, corresponding to a molar composition of Me (Zn/Cu): Im: bIm ≈ 4: 7: 1, with GVL and H_2O in a 1:1 (*v*/v) ratio, were added to a 10 ml stainless steel grinding jar, together with two 10 mm stainless steel grinding balls (Table S1). The grinding jar was sealed and shaken at 30 Hz for 30 min on a Retsch MM400 mixer mill. After grinding, the jars were opened and the powder extracted. Centrifugation was used to isolate the products, which were then washed with ethanol and dried overnight at 60 °C. The so prepared samples used for further analyses were named ZIF-62 and n% Cu-62, where n = 5, 10, 15, or 20 mol%, corresponding to substitution of 0.05, 0.10, 0.15, or 0.20 mmol of Cu for Zn in the synthesis mixture (with the total metal content fixed at 1.00 mmol). Additional synthesis information can be found in the supporting information.

To further explore how robust Cu^{2+} incorporation is under varying conditions, we carried out several additional syntheses using different copper sources and solvents. The details of these experiments are summarized in supporting information.

2.3. Test of glass fabrication

About 20 mg of the samples were pressed into pellets using a stainless-steel mould (0.8 cm in diameter) pressed in a hydraulic press for 1 min with a pressure of 1 t. Pelletized samples were placed in a ceramic crucible and then into an argon-purged muffle furnace before being heated at 10 °C/min to 350 °C. Once the temperature was reached, the furnace was turned off and the samples were allowed to cool naturally (under argon) to room temperature. The so prepared samples used for further analyses were named a_g ZIF-62 and a_g Cu-62.

2.4. Materials characterization

Powder X-ray diffraction data were acquired with a PANanalytical X'Pert PRO high-resolution diffractometer using CuKα1 radiation (1.5406 Å) in the 2θ range from 5 to 50° (100 s per step of 0.033°) with a fully open X'Celerator detector. The diffractograms were analysed by X'Pert HighScore Plus 4.9 Program with built in Rietveld refinement option.

Thermogravimetric analysis was performed using a TA Instruments Q5000. Measurements were performed in a continuous air stream (25 ml/min air, 10 ml/min Ar), with samples heated from 25 °C to 750 °C at a rate of 10 °C/min. DSC analysis of all samples was performed using a TA Instruments Q2000 MDSC. The samples were placed in an aluminium crucible on a DSC sample holder at room temperature. The samples were heated at 10 °C/min to 450 °C. After cooling to room temperature at 10 °C/min, the second upscan was performed using the same procedure as the first. Data analysis was performed using TA Instruments' TRIOS software.

Morphology and size of the crystals were determined by scanning electron microscopy using a Zeiss Supra 35 VP microscope with an electron high tension voltage of 1.00 kV and an aperture size of 30.00 µm. An energy-dispersive X-ray microanalyzer (EDX) connected to a scanning electron microscope was used to determine the presence of copper in gold-coated samples.

Proton NMR was recorded using an AVANCE NEO Bruker 400 MHz spectrometer at room temperature. Approximately 1.5 mg of each sample was digested in a mixture of DCl (35%)/D_2O (0.1 ml) and DMSO (0.5 ml). Data analysis was performed using TopSpin software package.

Solid-state NMR experiments were performed on a 600 MHz Varian spectrometer equipped with a 1.6 mm HXY FastMAS probe, operating at a MAS frequency of 20 kHz. The Larmor frequencies were 599.31 MHz (^{1}H), 150.81 MHz (^{13}C), and 40.50 MHz (^{15}N). Chemical shifts were referenced to tetramethylsilane (TMS) for ^{1}H and ^{13}C, and to nitromethane for ^{15}N. ^{1}H and ^{13}C spectra were collected using a Hahn-echo pulse sequence, with the interpulse delay set to one rotor period. For ^{1}H MAS experiments, the excitation pulse duration was 1.5 µs, with 64 scans accumulated and a 1 s recycle delay. ^{1}H–^{13}C and ^{1}H–^{15}N CP-MAS spectra were acquired with 100,000 scans, a recycle delay of 0.5 s, and a 4 ms ramped-amplitude contact pulse. Protons were excited with a 90° pulse of 1.5 µs.

Direct-excitation ^{13}C MAS experiments were carried out with 1.7 µs excitation pulses, 32 scans, and variable recycle delays (1–500 s). Single-pulse ^{1}H MAS experiments were performed with 1.5 µs excitation pulses, 8 scans, and variable recycle delays (0.1–10 s).

Elemental composition was determined by inductively coupled plasma optical emission spectroscopy (ICP-OES) using a Varian 715-ES instrument (GMP certified). Approximately 10 mg of sample was digested in concentrated HNO_3 and diluted with deionized water prior to analysis. The concentrations of Zn and Cu were determined against multi-element calibration standards and are reported as weight percentages relative to total sample mass.

CO_2 sorption data were collected using an Anton Paar IQ3 adsorption

analyser. For each measurement, a fresh sample batch was used and outgassed prior to analysis at 150 °C for 10 h with a heating rate 10 °C/min. The specific surface area was determined using BET theory from CO_2 isotherms measured at 273 K in the relative pressure range 0.017–0.027, showing a linear correlation (Fig. S9).

Diffuse reflectance UV–Vis (DR UV–Vis) spectra were recorded on a PerkinElmer Lambda 650 UV–Vis spectrophotometer equipped with an RSA-PE-19 Praying Mantis accessory for powdered samples. Spectra were collected in the range of 200–900 nm at room temperature, using $BaSO_4$ as a white reflectance standard for background correction.

Fourier transform infrared (FT-IR) spectra were collected on a Bruker ALPHA II spectrometer equipped with a diamond ATR module. Measurements were performed in the range 4000–400 cm^{-1} at room temperature, with a spectral resolution of 4 cm^{-1} and 32 scans averaged per spectrum.

Raman spectra were collected using a WITec Alpha 300RA confocal Raman/AFM microscope equipped with a 532 nm excitation laser. The laser power at the sample surface was maintained between 10 and 15 mW and focused through a 50× objective (NA = 0.8). The spectral integration time was set to 1 s per acquisition.

Cu and Zn K-edge X-ray absorption spectra (XAS) of ZIF-62, 10% Cu-62, and 20% Cu-62 samples, as well as their reference compounds, were recorded in transmission detection mode on the P65 beamline at PETRA III (DESY, Hamburg). A Si(111) double crystal monochromator was used, providing an energy resolution of approximately 1 eV at 9 keV. Higher-order harmonics were effectively eliminated by a flat mirror. Three repetitions of XAS spectra were measured in continuous detection mode in a short 3 min scans. The intensity of the monochromatic X-ray beam was measured with ionization detectors filled with 1020 mbar of suitable absorption gas mixtures to absorb a total of 16% (10% Ar, 90% N_2), 54% (15% Ar, 85% N_2), and 90% (Kr), respectively.

The absorption spectra were measured in the energy region from −150 eV to +1000 eV relative to the Cu and Zn K-edges (8978 eV and 9695 eV, respectively). Exact energy calibration was established using absorption measurements on 5 μm thick Cu and Zn metal foils placed between the second and third ionization detectors. The absolute energy reproducibility of the measured spectra was ±0.05 eV. The sample powders and reference compounds (Cu acetate, Cu_2O, CuO, and ZnO) were homogeneously mixed with approximately 50 mg of boron nitride and prepared as homogeneous pellets with an optimal total absorption thickness of about 1.5 above the Cu or Zn K-edge. The pellets were placed in the monochromatic beam after the first ionization detector. The analysis of X-ray absorption near edge structure (XANES) and extended X-ray absorption fine structure (EXAFS) spectra was performed with the DEMETER (IFEFFIT) program package [43] in combination with the FEFF8 program code [44] for ab initio calculation of photoelectron scattering paths.

3. Results and discussion

In the attempt to incorporate copper into the ZIF-62 structure, Zn $(OAc)_2{\cdot}2H_2O$ was partly replaced with $Cu(OAc)_2{\cdot}H_2O$ during mechanochemical synthesis (5–20 wt% of $Cu(OAc)_2{\cdot}H_2O$). The XRD patterns of the products exhibited general agreement with the calculated [45] and synthesized pure ZIF-62 patterns, with some observable differences in peak intensities and shifts in peak positions. This suggests that the samples retained the long-range structural features of ZIF-62 (Fig. 1). The analysis of XRD patterns further showed that the samples retained the long-range symmetry of ZIF-62 (Fig. S1), while the observed differences in unit cell parameters (Table S2) could be assigned to the expansion of the unit cell after copper loading. The comparison of the Full Width at Half Maximum (FWHM) of the initial peaks indicated a significant degree of crystallinity also in the mixed-metal samples. Additionally, XRD revealed the presence of minute amounts of ZnO impurities in samples. Based on these promising structural similarities, further analysis was attempted to determine whether Cu^{2+} was successfully incorporated into the framework rather than existing as surface species or even forming additional phases.

On the other hand, to evaluate the robustness of Cu^{2+} incorporation, additional synthesis approaches were explored (Fig. S2). Mechanochemical synthesis using CuO and/or $Cu(OAc)_2{\cdot}H_2O$ as a precursor failed to yield Cu-loaded ZIF-62. When $Cu(OAc)_2$ and the linkers were dissolved in butanol, the resulting phase was consistent with $Cu(Im)_2$ (ZIF-Cu-1), aligning with the reported literature structure [36]. However, when attempting to reproduce the literature synthesis of this material using $CuSO_4$, either with imidazole alone or a combination of imidazole and benzimidazole, the reaction yielded a completely different crystalline phase, distinct from both ZIF-Cu-1 and ZIF-62 (Fig. S2).

A similar structural deviation was observed for several other solvothermal synthesis approaches. When $CuSO_4$ was dissolved in GVL, where the resulting material exhibited the same crystalline structure regardless of whether imidazole or a mixture of imidazole and benzimidazole was used, yet remained distinct from all previously obtained phases. Meanwhile, when $Cu(OAc)_2$ was dissolved in GVL, the material was amorphous, regardless of the linker composition, suggesting that

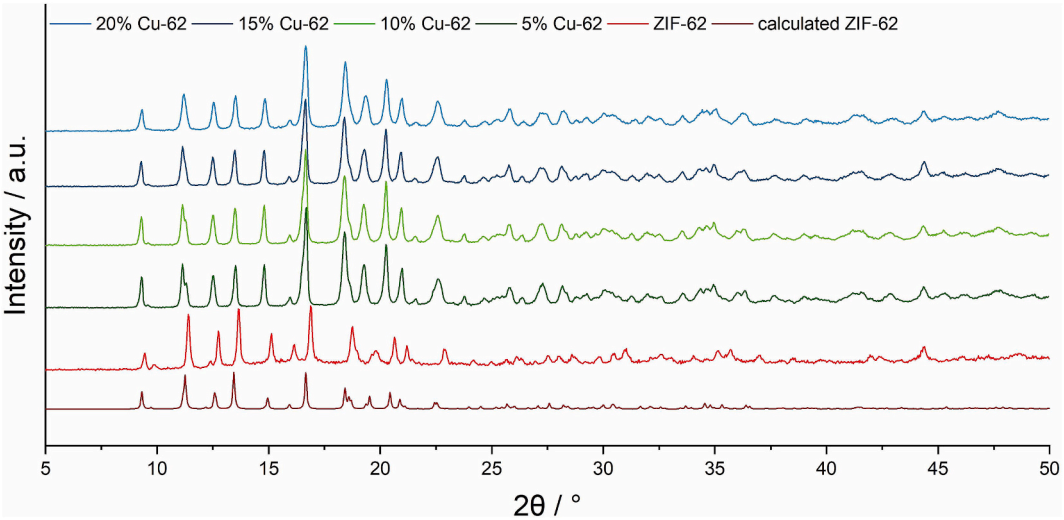

Fig. 1. PXRD of calculated, ZIF-62 and shown alongside with the XRD patterns of unmodified ZIF-62 and Cu-modified ZIF-62 (n% Cu-62) obtained by mechanochemical synthesis.

metal source choice strongly influences the final structure. Additionally, when $Cu(NO_3)_2$ was used in butanol without benzimidazole, yet another distinct crystalline phase was obtained, differing from all other synthesized materials (Fig. S2). These results suggest that Cu^{2+} does not simply substitute Zn^{2+} in the ZIF-62 framework but instead directs crystallization into alternative structures depending on the synthesis conditions. The variability in products obtained from different Cu precursors and solvents highlights that Cu^{2+} behaves differently from Zn^{2+} during framework assembly.

The results of various synthesis protocols are consistent with the coordination chemistry of Cu(II), which, unlike Zn^{2+} fixed in tetrahedral ZnN_4 nodes, can adopt 4-, 5-, or 6-coordinate geometries [37,46], often stabilized in square-planar or Jahn–Teller-distorted octahedral environments [47]. Because of this mismatch, direct substitution is expected to be challenging, and careful structural analysis was required. For this reason, most of the characterization was focused exclusively on the mechanochemically synthesized Cu-62 samples, which reproducibly retained the structural features of ZIF-62 and provided phase-pure material for comprehensive study. All subsequent analyses, including solid-state NMR, FT-IR, Raman, DR UV-Vis, ICP-OES, and XAS, were therefore performed on the n% Cu-62 ($n = 5$ to 20) series to determine the nature and extent of Cu^{2+} incorporation.

To verify the linker ratio in the mechanochemically produced pure and copper-loaded ZIF-62, solution proton NMR was conducted. All crystalline samples and resultant glasses from the mixed metal series, produced through mechanochemical synthesis, exhibited a consistent linker ratio of Im:bIm = 6:1 (Fig. S3). This ratio is slightly lower than the nominal 7:1 ratio typically reported [48] for ZIF-62, but its persistence across all samples indicates that mechanochemical synthesis reproducibly yields this composition. The sustained linker ratio in the ZIF-62 (Zn/Cu) series of crystalline samples allowed for meaningful correlations between their melting temperatures and the glass transitions of the quenched glasses.

Thermogravimetric analysis (TGA) and differential scanning calorimetry (DSC) were conducted to examine the melting behaviour of mechanochemically synthesized pure ZIF-62 and copper loaded ZIF-62 (Fig. S4). Interestingly, the melting temperature (T_m) of mechanochemically produced pure ZIF-62 was found to be lower (380 °C) than that of previously reported [48] solvothermally produced samples with the same chemical composition (440 °C). The glass transition temperature (T_g) of pure ZIF-62 aligned with prior reports [48] of solvothermally produced ZIF-62, registering a midpoint at 330 °C. The addition of copper resulted in a decrease in T_m to 350 °C and T_g to 310 °C. Although spectroscopic analysis later indicates that Cu is not incorporated directly into the tetrahedral framework nodes of ZIF-62, the Cu-loaded samples consistently exhibit reduced melting and glass transition temperatures compared to pristine ZIF-62. In mixed-metal Zn/Co ZIF-62 systems, similar reductions in T_m and T_g have previously been attributed to framework substitution and altered node–linker interactions arising from structural mismatch between metal ions. [49] In the present system, however, the exact origin of the thermal behaviour remains uncertain, as the spectroscopic results do not support direct Cu substitution into the framework nodes. Nevertheless, non-framework Cu species may still influence thermal behaviour through increased local disorder, modified interparticle interactions, perturbation of linker dynamics, or interactions within surface and pore environments. Additionally, the substantially smaller crystallite sizes observed for mechanochemically synthesized samples likely contribute to the reduced melting temperatures relative to previously reported solvothermal ZIF-62 materials. The observed thermal shifts therefore likely arise from a combination of particle-size effects and interactions associated with non-framework Cu species.

Importantly, after melt-quenching, all Cu-containing samples were X-ray amorphous, and no ZnO reflections were detected (Fig. S5), in contrast to previous reports [40,50] where ZIF-62 glasses exhibited ZnO contamination upon melting.

TGA under air revealed that mechanochemically produced pure ZIF-62 is stable up to ~400 °C, while Cu-62 samples retain stability up to ~450 °C. By 750 °C, the total mass losses were 53% for pure ZIF-62 and 56% for the Cu-loaded samples, indicating higher metal-to-linker ration in copper-loaded samples. All samples exhibited an additional ~5% weight loss around 200 °C, attributed to the removal of adsorbed water or residual linker rather than framework decomposition.

SEM imaging of the mechanochemically produced pure and copper-loaded ZIF-62 unveiled particle sizes ranging from 1 μm to sub-100 nm (Fig. S6) significantly smaller than ZIF-62 particles produced via solvothermal methods, which typically exhibit sizes on the 10 μm scale. Consequently, the reduced melting temperature of mechanochemically produced ZIF-62 is attributed to the smaller particle size compared to solvothermally produced ZIF-62. Energy-dispersive X-ray spectroscopy (EDS) was employed to examine the spatial distribution of Zn and Cu within the samples. All Cu-loaded samples exhibited a relatively homogeneous Cu distribution throughout the material, without evidence of large Cu-rich segregated regions (Fig. S6). However, due to the spatial resolution limits of SEM-EDS, the measurements cannot distinguish whether Cu species are framework-incorporated, surface-associated, or pore-confined. Furthermore, ICP-OES was employed to assess the copper content in 10% Cu-62 and 20% Cu-62 after digestion in an HNO_3 solution (Table S3).

Based on ICP-OES results, the Cu content in the samples prepared with nominal 10 mol% and 20 mol% Cu loadings was determined to be 1.00 wt% (~3.3 mol%) and 1.99 wt% (~6.7 mol%), respectively. This suggest that majority of Cu does not actually substitute Zn in the ZIF-62 framework, but rather remains on the particle surface or inside the pores as loosely bound Cu species. These are easily removed during washing, so only a small, more strongly attached fraction remains in the final product, which explains the lower Cu content measured by ICP compared to the nominal loading. Porosity of the ZIF-62-based materials was assessed by CO_2 sorption isotherms collected at 273 K (Fig. S8), a probe particularly suitable for evaluating ultramicroporous regions in ZIFs and related MOFs due to the diffusion limitations commonly encountered for N_2 adsorption at 77 K. CO_2 sorption is employed primarily to compare relative uptake and trends in accessible microporosity between samples rather than to extract absolute textural parameters, since specific CO_2–framework interactions can lead to overestimation of surface area and pore volume values. [50,51] All samples exhibited characteristic Type I isotherms, confirming the presence of microporosity. A progressive decrease in CO_2 uptake and calculated surface area was observed with increasing nominal Cu loading, decreasing from 446 m^2/g for pristine ZIF-62 to 216 m^2/g for 20% Cu-62 (Fig. S9, Table S4). This reduction in pore accessibility is consistent with Cu-containing species affecting surface and/or pore environments rather than direct substitution within the tetrahedral framework nodes.

The electronic environment of the metals was further investigated by diffuse reflectance ultraviolet–visible spectroscopy (DR UV–Vis), as depicted in Fig. 2. In pure Zn ZIF-62 sample, a prominent absorption peak at 220 nm was observed, indicative of intra-ligand charge transfer. [52] The presence of an absorption band around 370 nm signalled the aggregation leading to the formation of ZnO particles. The pure Zn-based ZIF-62 sample exhibited also a weak absorption at 300 nm, attributed to ligand-to-metal charge transfer [53] (LMCT), with no absorbance in the visible region, consistent with its white colour.

In contrast, all Cu-62 samples exhibited additional broad absorption bands extending across the visible spectral region compared to pristine ZIF-62. These bands are consistent with ligand-field d–d transitions associated with Cu(II) ions reported in the literature. [17,52] The intensity of the visible-region absorption generally increased with increasing nominal Cu loading, consistent with a higher concentration of Cu-containing species in the samples.

In the ^1H–^{13}C CPMAS NMR spectra of copper-loaded samples (Fig. 3), the peaks within the 144–142 ppm and 126–123 ppm ranges are

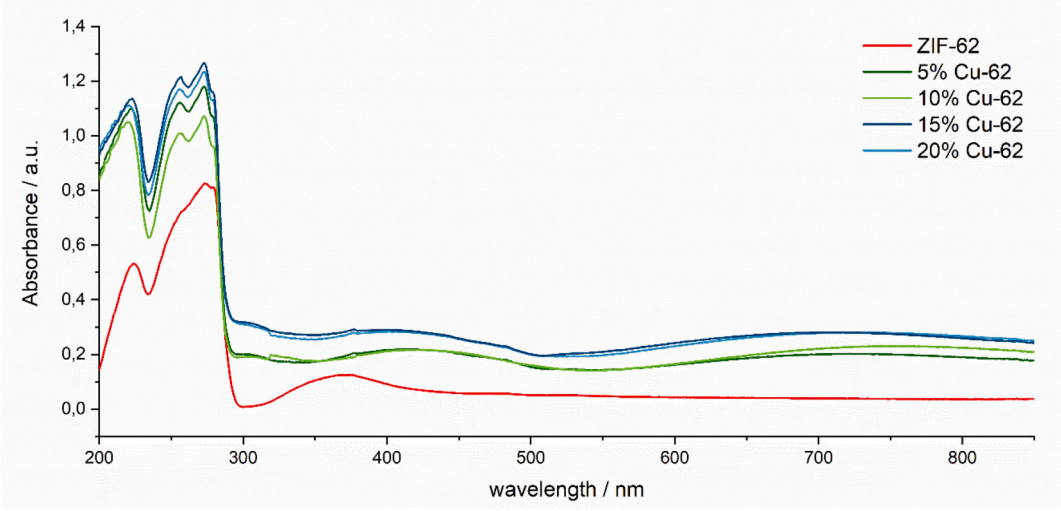

Fig. 2. DR UV–Vis spectra of pure ZIF-62 and n% Cu-62 sample.

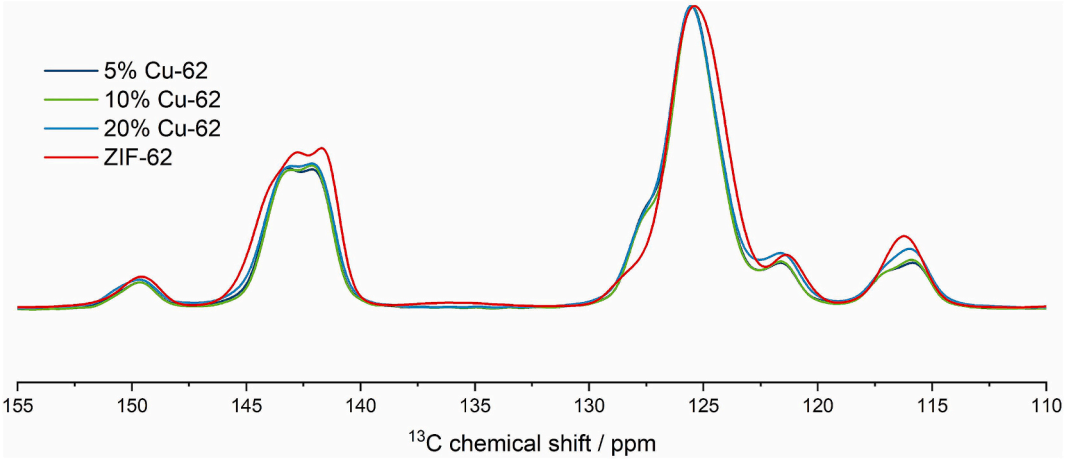

Fig. 3. ^{1}H–^{13}C CPMAS NMR spectra of pure ZIF-62 and n% Cu-62 samples.

attributed to the NCN and NCC carbons of imidazole, respectively. Peaks resonating at 149.2 ppm, 121.8 ppm, and 117–115 ppm are assigned to the NCN, CHCHCN, and CHCHCN carbons of benzimidazole.

The ^{15}N spectra (Fig. S10) also exhibit characteristic peaks for both linkers. Because Cu(II) is paramagnetic, framework incorporation of Cu into metal nodes would be expected to influence nearby linker nuclei

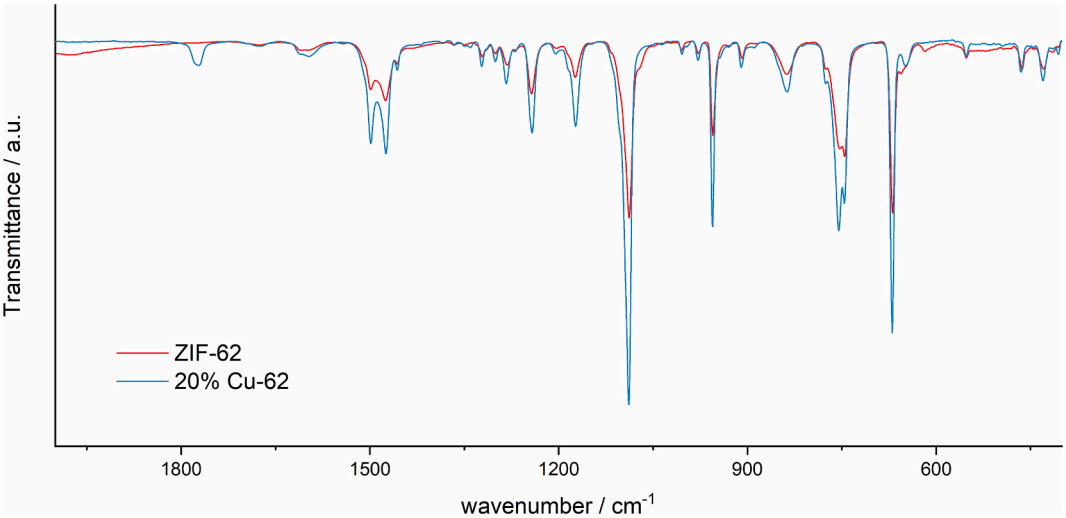

Fig. 4. FT-IR spectra of pure ZIF-62 and 20% Cu-62 sample.

through paramagnetic shifts, line broadening, and/or enhanced relaxation effects. In the present spectra, no significant chemical shift changes are observed relative to pristine ZIF-62, indicating that Cu does not substantially change the average linker coordination environment. The main difference is instead observed in the relaxation behaviour (Fig. S11.), with shorter recycle delays in the Cu-loaded samples, consistent with the presence of paramagnetic Cu species located near, but not necessarily incorporated into, the framework. [54]

The Fourier transform infrared (FT-IR) spectra of pure ZIF-62 and 20% Cu-62 sample are displayed in Fig. 4, while the corresponding band assignments are summarized in Table S5 in the SI. The peak at 423 cm^{-1} corresponds to the Zn—N stretching mode, indicating that zinc atoms are coordinated with nitrogen atoms in the linkers to form the ZIF framework structure [55]. The absorption bands observed in the range of 1100–1300 cm^{-1} are assigned to C—H vibrations, while the peak around 1320 cm^{-1} is attributed to C—N bonding. Peaks at 1556 and 1618 cm^{-1} are associated with C═C stretching vibrations, and the peak at 1246 cm^{-1} confirm the C—C vibrations within the imidazole and benzimidazole ring. [56,57] Importantly, upon analysis, no significant differences or additional peaks were observed in the spectra of the Cu-62 samples compared to the pure ZIF-62. The absence of significant spectral changes indicates that copper does not substantially perturb the vibrational environment of the ZIF-62 framework. However, FTIR results alone cannot fully exclude low levels of framework substitution, and therefore these observations were interpreted together with complementary techniques.

The Raman spectra of ZIF-62 and 20% Cu-62 are presented in Fig. 5, and they agree well with the literature [29,58]. The peak at 1278 cm^{-1} is the result of symmetric stretching in the organic linker. In the low wavenumber range of 100–400 cm^{-1}, rocking δ(Zn—N), asymmetric (Zn—N), and symmetric (Zn—N) stretching vibrations can be observed. There is no discernible difference between the copper-loaded samples spectra, and the formation of a Cu—N bond is not visible from the spectra, suggesting that Cu presence does not significantly alter the framework structure. Raman measurements were not possible for the glassy copper-loaded material, which merely gave fluorescence.

Cu and Zn K-edge XAS analysis was used to determine the valence state and local symmetry, as well as the local structure around metal cations in the pure and Cu-modified ZIF-62. Different local environments of metal cations lead to different K-edge profiles in the XANES (X-ray absorption near edge structure) region, and the energy position of the corresponding metal K-edges correlate with the valence state of the metal cations in the sample. [59] The normalized Cu and Zn K-edge XANES spectra of the samples are shown together with reference copper and zinc compounds (for copper: Cu metal foil, Cu_2O as a reference for Cu^{1+}, and CuO and Cu acetate ($Cu(OAc)_2$) as references for Cu^{2+}; for zinc: Zn metal foil and ZnO as a reference for Zn^{2+}) with different valence states and local coordination in Fig. S12 and Fig. S13 in Supplementary information. The Cu K-edge edge positions in case of 10% Cu-62 and 20% Cu-62 samples are similar to that in the spectra of the Cu acetate and CuO which shows that they contain predominantly Cu^{2+} cations. For the ZIF-62, 10% Cu-62 and 20% Cu-62 samples, the Zn K-edge is at the position of ZnO, so Zn cations in the samples are in the 2+ oxidation state.

Cu and Zn K-edge EXAFS (extended X-ray absorption fine structure) analysis is used to directly probe the local structure around Cu and Zn cations in the ZIF-62 and Cu-modified ZIF-62 samples. Structural parameters of the average local cation neighbourhood (the type and average number of neighbours, the radii and Debye–Waller factor of neighbour shells) are quantitatively resolved from the EXAFS spectra by comparing the measured EXAFS signal with the model signal, constructed ab initio with the IFEFFIT program code. [44] The type of atomic species of the neighbours is identified in the fit by their specific scattering factor and their phase shift.

Cu K-edge XANES results showed that the local coordination in the samples is different to the Cu precursor used in the synthesis, Cu acetate. Differences in average local structures around Cu cations in the samples are visible by qualitative comparison of Fourier transform magnitude of k^3-weighted Cu K-edge EXAFS spectra (Fig. 6, black solid lines).

For the quantitative Cu K-edge EXAFS analysis of the samples, two models were constructed. For the reference Cu acetate, the model was based on Cu acetate monohydrate with a $P2_1/m$ space group and a paddle-wheel-like structure. The model included five single scattering paths up to 3.2 Å. Cu is coordinated to four (2 + 2) O atoms at a distance of 1.9 Å and one O atom at 2.4 Å in the first coordination shell, one Cu atom at 2.5 Å and four C atoms at 2.9 Å in the second shell, and another Cu atom at 3.2 Å in the third shell (Table S6). Ten variable parameters were used: the shift of the energy origin of the photoelectron (ΔE_o), the distances (R) of each scattering path and the Debye–Waller (σ^2) factors for each path. The amplitude reduction factor ($S_0^2 = 0.84$) was retained from the fit of the first shell, presuming Cu is coordinated to 4 + 2 oxygen atoms. The coordination numbers were kept fixed at the crystallographic values. A good fit was obtained for the reference in the R-range of 1.2–3.2 Å and in the k-range of 3–10 $Å^{-1}$ (Fig. 6, red dashed line). The best-fit parameters are listed in the Supplementary Information file (Table S6). Although the refined Debye–Waller (DW) factors do not strictly exhibit a monotonic increase with interatomic distance, this behaviour is attributed primarily to the strong parameter correlations

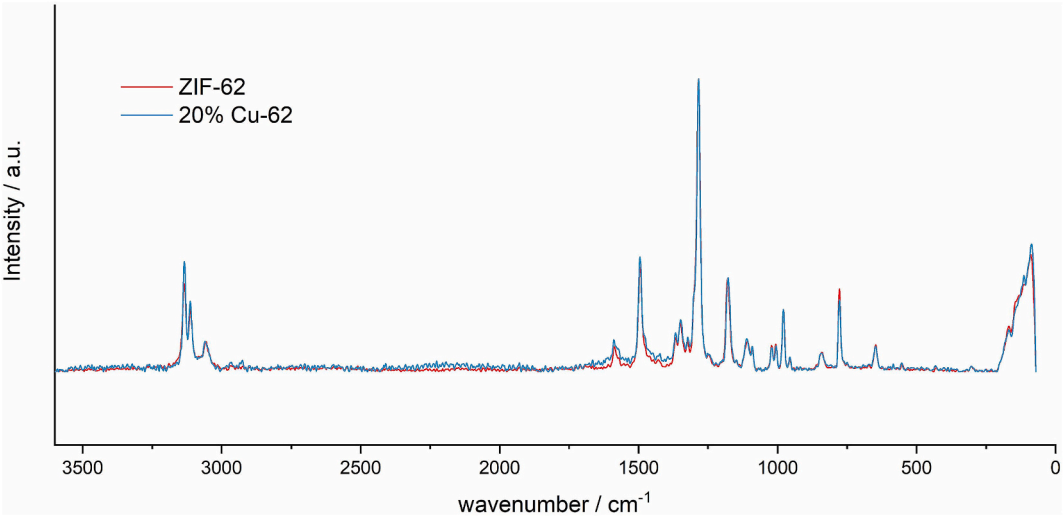

Fig. 5. Raman spectra of pure ZIF-62 and 20% Cu-62 sample.

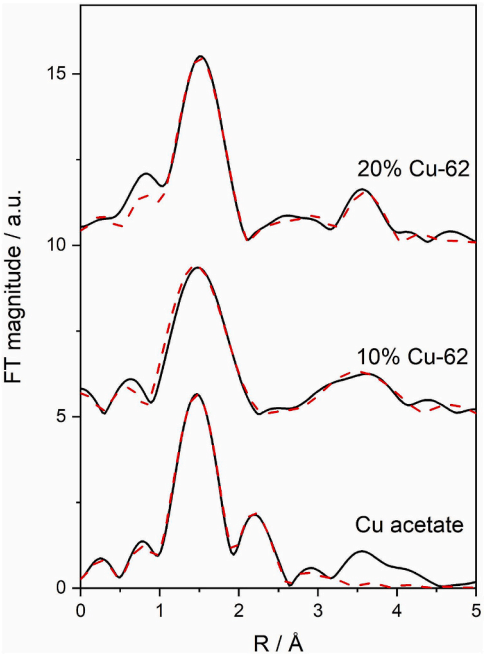

Fig. 6. Fourier transform magnitude of k^3-weighted Cu K-edge EXAFS spectra for 10% Cu-62 and 20% Cu-62 samples together with reference Cu acetate, calculated in the *k*-range of 3.5–10 Å^{-1}. The *R*-range used was 1.2–3.2 Å for Cu-acetate and 1.2–4.2 Å for the 10% Cu-62 and 20% Cu-62 samples. The solid black line represents the experimental data, and the dashed red line represents the best-fit EXAFS model. The spectra are displaced vertically for clarity. (For interpretation of the references to colour in this figure legend, the reader is referred to the web version of this article.)

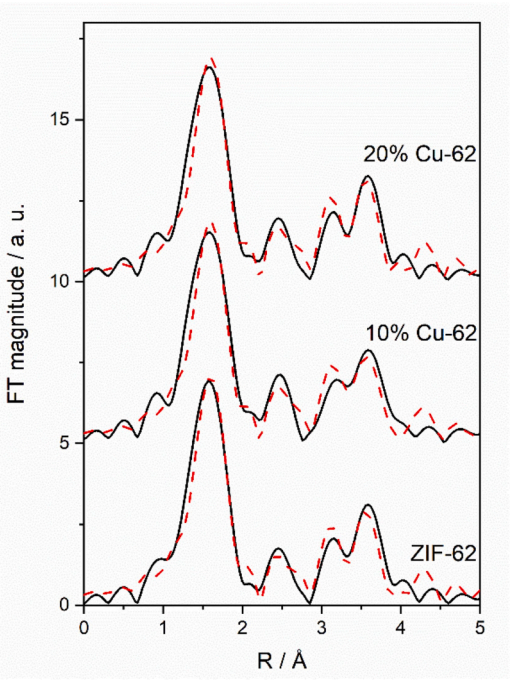

Fig. 7. Fourier transform magnitude of k^3-weighted Zn K-edge EXAFS spectra of ZIF-62, 10% Cu-62 and 20% Cu-62 sample, calculated in the *k*- and *R*- range of 3–12 Å^{-1} and 1.2–4.3 Å, respectively. The solid line represents the experiment, and the dashed line represents the best-fit EXAFS model. The spectra are displaced vertically for clarity.

inherent in EXAFS fitting rather than indicating an unphysical structural model.

For the 10% Cu-62 and 20% Cu-62 samples, a modified Cu-imidazole structure was first adopted where the first shell is composed of four C or N or O atoms at about 2.0 Å. In XAS, carbon, nitrogen and oxygen atoms cannot be distinguished due to their similar scattering factors. In the second shell, eight carbon atoms are at about 3.0 Å. In the third shell, another eight carbon atoms are at 4.2 Å. The model included three scattering paths with 10 variable parameters: the coordination numbers (*N*), the distances to neighbour atoms (*R*) and the Debye–Waller (σ^2) factors for each scattering path were varied.

The shift of the energy origin of the photoelectron (ΔE_o) was common to each path. The amplitude reduction factor ($S_0^2 = 0.84$) was taken from the fit of the reference Cu acetate. A good fit was obtained for the samples in the *R*-range of 1.2–4.2 Å and in the *k*-range of 3–10 Å^{-1} (Fig. 6, red dashed line). The best-fit parameters are listed in the Supplementary Information file (Table S7).

Cu K-edge XAS analysis shows that the environment around Cu atoms changes during mechanochemical synthesis. During synthesis, the initial precursor, Cu acetate with a paddle-wheel-like structure, is broken, and Cu most probably becomes surrounded by C or N atoms from imidazolate-based linkers. Cu is coordinated to 5 ± 1 atoms with high disorder (high Debye-Waller factor), which are further bound to C or N atoms. Because Cu adopts coordination environments distinct from the tetrahedral Zn sites of ZIF-62, the Cu species are more likely associated with surface and/or pore environments interacting with imidazolate-based linkers, in agreement with the combined spectroscopic and sorption results.

Zn K-edge EXAFS analysis is used to directly probe the local structure around Zn cations in the pure ZIF-62 sample and in Cu-modified ZIF-62 with 10% and 20% Cu. Comparison of the Fourier transform magnitude of k^3-weighted Zn K-edge EXAFS spectra (Fig. 7, black solid lines) shows that, qualitatively, there are no differences between the ZIF-62 and Cu-modified ZIF-62 samples.

For the quantitative Zn K-edge EXAFS analysis, the FEFF model was constructed based on the modified ZIF-62 crystal structure with Pbca space group, which included three single scattering paths up to 4.3 Å with nine variable parameters: the shift of the energy origin of the photoelectron (ΔE_o), the coordination number of the second and third coordination shells, the coordination shell distance (*R*), and the Debye–Waller (σ^2) factors for all paths. The amplitude reduction factor ($S_0^2 = 0.90$) is retained from the fit of the first shell in the pure ZIF-62 sample, presuming Zn is coordinated to four nitrogen atoms. Zn is coordinated to four N atoms at a distance of 2.0 Å in the first coordination sphere, eight C atoms in the range from 3.0 Å to 3.4 Å in the second shell, and four C atoms at about 4.0 Å and four N atoms at 4.2 Å in the third coordination sphere. Good fits are obtained for the pure and Cu-modified ZIF-62 samples in the same in the *R*-range of 1.2–4.3 Å and in the *k*-range of 3–13 Å^{-1} (Fig. 7, red dashed line). The best-fit parameters are listed in the Supplementary Information file (Table S7).

XAS results show that the average coordination number (*N*), bond distances (*R*) and Debye−Waller factor (σ^2) around Zn cations remain unchanged throughout the Cu modification of the ZIF-62 sample. This indicates that the mechanosynthetic approach does not affect the first-nearest neighbour tetrahedral coordination of Zn atoms in ZIF-62 and retained the long-range structural features of ZIF-62. This is in agreement with the XRD results.

The XAS results, in conjunction with the structural deviations observed in solvothermal synthesis attempts, emphasize the strong influence of metal-ligand coordination preferences on MOF formation. Unlike Zn^{2+}, which readily forms tetrahedral Zn—N bonds within ZIF-62, Cu^{2+} frequently stabilises in five or higher coordinate geometries, such as the paddlewheel unit of the HKUST-1 [60]. Furthermore, DFT studies [61] show that Cu—N bonds are more rigid than Zn—N bonds, making it challenging for Cu^{2+} to adapt to ZIF-62's flexible tetrahedral coordination. As a result, Cu^{2+} does not entirely integrate into the framework, instead, it remains a surface-adsorbed species, influencing

the material's thermal properties.

4. Conclusion

This study examined the incorporation of Cu^{2+} into ZIF-62 using mechanochemical and solvothermal synthesis approaches. Mechanochemical synthesis yielded crystalline materials retaining the ZIF-62 topology; however, combined spectroscopic, sorption, and structural analyses consistently indicated that Cu does not substitute Zn within the tetrahedral framework nodes under the investigated conditions. Instead, Cu adopts alternative coordination environments and is more likely associated with surface and/or pore environments within the mechanochemically synthesized Cu-62 materials. Despite the absence of direct framework substitution, Cu addition progressively reduced the accessible microporosity, melting temperature, and glass transition temperature of the mechanochemically synthesized Cu-62 series, demonstrating that non-framework copper can still measurably influence the bulk properties of ZIF-derived materials. In contrast, additional solvothermal synthesis attempts produced alternative crystalline or amorphous phases rather than Cu-modified ZIF-62, highlighting the strong influence of Cu coordination chemistry, precursor selection, and synthesis conditions on framework formation. Overall, these findings demonstrate that Cu incorporation into ZIF-62 is strongly limited under the mechanochemical and solvothermal conditions explored in this work and highlight the importance of precursor selection and metal-ligand coordination preferences in the design of mixed-metal MOFs and MOF glasses.

CRediT authorship contribution statement

Marija Švegovec: Writing – original draft, Visualization, Investigation, Formal analysis, Data curation, Conceptualization. **Andraž Krajnc:** Writing – review & editing, Validation, Supervision, Conceptualization. **Ksenija Maver:** Writing – review & editing, Visualization, Investigation, Formal analysis, Data curation. **Nataša Zabukovec Logar:** Writing – review & editing, Validation, Supervision, Funding acquisition, Conceptualization.

Declaration of competing interest

The authors declare that they have no known competing financial interests or personal relationships that could have appeared to influence the work reported in this paper.

Acknowledgment

We acknowledge access to synchrotron radiation facility at DESY (Hamburg, Germany), PETRA III (beamline P65, project I-20221241 EC). We also acknowledge support by the Slovenian Research and Innovation Agency (Research Core Funding No. P1-0021 and P1-0418 and Research Projects No. J1-50020, J7-4636 and GC-0003. The authors would like to thank Mojca Opresnik for SEM/EDX measurements, Edi Kranjc for XRD measurements, Kristijan Lorber for UV–Vis measurements, Klara Klemenčič for CO_2 sorption measurements, Nigel Van de Velde for Raman measurements and Iris Štucin and Breda Novak for ICP-OES measurements.

Appendix A. Supplementary data

Supplementary data to this article can be found online at https://doi.org/10.1016/j.rechem.2026.103620.

Data availability

Data will be made available on request.

References

[1] O.M. Yaghi, N.W. Ockwig, H.K. Chae, M. Eddaoudi, J. Kim, Reticular synthesis and the design of new materials. www.nature.com/nature, 2003.
[2] K.W. Chapman, G.J. Halder, P.J. Chupas, Pressure-induced amorphization and porosity modification in a metal-organic framework, J. Am. Chem. Soc. 131 (2009) 17546–17547, https://doi.org/10.1021/ja908415z.
[3] C. Zhou, L. Longley, A. Krajnc, G.J. Smales, A. Qiao, I. Erucar, C.M. Doherty, A. W. Thornton, A.J. Hill, C.W. Ashling, O.T. Qazvini, S.J. Lee, P.A. Chater, N. J. Terrill, A.J. Smith, Y. Yue, G. Mali, D.A. Keen, S.G. Telfer, T.D. Bennett, Metal-organic framework glasses with permanent accessible porosity, Nat. Commun. 9 (2018), https://doi.org/10.1038/s41467-018-07532-z.
[4] F. Yang, W. Li, B. Tang, Facile synthesis of amorphous UiO-66 (Zr-MOF) for supercapacitor application, J. Alloys Compd. 733 (2018) 8–14, https://doi.org/10.1016/j.jallcom.2017.10.129.
[5] I. Ahmed, M.M.H. Mondol, M.J. Jung, G.H. Lee, S.H. Jhung, MOFs with bridging or terminal hydroxo ligands: applications in adsorption, catalysis, and functionalization, Coord. Chem. Rev. 475 (2023), https://doi.org/10.1016/j.ccr.2022.214912.
[6] W. Fan, X. Wang, B. Xu, Y. Wang, D. Liu, M. Zhang, Y. Shang, F. Dai, L. Zhang, D. Sun, Amino-functionalized MOFs with high physicochemical stability for efficient gas storage/separation, dye adsorption and catalytic performance, J. Mater. Chem. A Mater. 6 (2018) 24486–24495, https://doi.org/10.1039/c8ta07839d.
[7] S. Mallakpour, E. Nikkhoo, C.M. Hussain, Application of MOF materials as drug delivery systems for cancer therapy and dermal treatment, Coord. Chem. Rev. 451 (2022) 214262, https://doi.org/10.1016/J.CCR.2021.214262.
[8] A.C. McKinlay, R.E. Morris, P. Horcajada, G. Férey, R. Gref, P. Couvreur, C. Serre, BioMOFs: metal-organic frameworks for biological and medical applications, Angew. Chem. Int. Ed. 49 (2010) 6260–6266, https://doi.org/10.1002/anie.201000048.
[9] Y. Wang, H. Jin, Q. Ma, K. Mo, H. Mao, A. Feldhoff, X. Cao, Y. Li, F. Pan, Z. Jiang, A MOF glass membrane for gas separation, Angew. Chem. Int. Ed. 59 (2020), https://doi.org/10.1002/anie.201915807.
[10] D. Li, A. Yadav, H. Zhou, K. Roy, P. Thanasekaran, C. Lee, Advances and applications of metal-organic frameworks (MOFs) in emerging technologies: a comprehensive review, Global Chall. 8 (2024), https://doi.org/10.1002/gch2.202300244.
[11] Y. Zhang, Y. Wang, H. Xia, P. Gao, Y. Cao, H. Jin, Y. Li, A hybrid ZIF-8/ZIF-62 glass membrane for gas separation, Chem. Commun. 58 (2022) 9548–9551, https://doi.org/10.1039/d2cc03179e.
[12] A. Awadallah-F, F. Hillman, S.A. Al-Muhtaseb, H.K. Jeong, Adsorption equilibrium and kinetics of nitrogen, methane and carbon dioxide gases onto ZIF-8, Cu10%/ZIF-8, and Cu30%/ZIF-8, Ind. Eng. Chem. Res. 58 (2019) 6653–6661, https://doi.org/10.1021/acs.iecr.8b05892.
[13] C. Ma, H. Liu, J. Qiu, X. Zhang, Bimetallic Zn/co-ZIF tubular membrane for highly efficient pervaporation separation of methanol/MTBE mixture, J. Membr. Sci. 638 (2021), https://doi.org/10.1016/j.memsci.2021.119676.
[14] D. Luo, Y.L. Peng, M. Xie, M. Li, A.A. Bezrukov, T. Zuo, X.Z. Wang, Y. Wu, Y.Y. Li, A.R. Lowe, M. Chorążewski, Y. Grosu, Z. Zhang, M.J. Zaworotko, X.P. Zhou, D. Li, Improving ethane/ethylene separation performance under humid conditions by spatially modified zeolitic imidazolate frameworks, ACS Appl. Mater. Interfaces 14 (2022) 11547–11558, https://doi.org/10.1021/acsami.2c00118.
[15] Z. Yang, Y. Belmabkhout, L.N. McHugh, D. Ao, Y. Sun, S. Li, Z. Qiao, T.D. Bennett, M.D. Guiver, C. Zhong, ZIF-62 glass foam self-supported membranes to address CH4/N2 separations, Nat. Mater. (2023), https://doi.org/10.1038/s41563-023-01545-w.
[16] C. Duan, Y. Yu, H. Hu, Recent progress on synthesis of ZIF-67-based materials and their application to heterogeneous catalysis, Green Energy Environ. 7 (2022) 3–15, https://doi.org/10.1016/J.GEE.2020.12.023.
[17] A. Schejn, A. Aboulaich, L. Balan, V. Falk, J. Lalevée, G. Medjahdi, L. Aranda, K. Mozet, R. Schneider, Cu2+−doped zeolitic imidazolate frameworks (ZIF-8): efficient and stable catalysts for cycloadditions and condensation reactions, Catal. Sci. Technol. 5 (2015) 1829–1839, https://doi.org/10.1039/c4cy01505c.
[18] C. Guo, Y. Zhang, X. Nan, C. Feng, Y. Guo, J. Wang, Efficient selective catalytic oxidation of benzylic CH bonds by ZIF-67 under eco-friendly conditions, Molecular Catalysis 440 (2017) 168–174, https://doi.org/10.1016/J.MCAT.2017.07.013.
[19] T.D. Bennett, Y. Yue, P. Li, A. Qiao, H. Tao, N.G. Greaves, T. Richards, G. I. Lampronti, S.A.T. Redfern, F. Blanc, O.K. Farha, J.T. Hupp, A.K. Cheetham, D. A. Keen, Melt-quenched glasses of metal-organic frameworks, J. Am. Chem. Soc. 138 (2016) 3484–3492, https://doi.org/10.1021/jacs.5b13220.
[20] H. Tao, T.D. Bennett, Y. Yue, Melt-quenched hybrid glasses from metal–organic frameworks, Adv. Mater. 29 (2017), https://doi.org/10.1002/adma.201601705.
[21] T.D. Bennett, J.C. Tan, Y. Yue, E. Baxter, C. Ducati, N.J. Terrill, H.H.M. Yeung, Z. Zhou, W. Chen, S. Henke, A.K. Cheetham, G.N. Greaves, Hybrid glasses from strong and fragile metal-organic framework liquids, Nat. Commun. 6 (2015), https://doi.org/10.1038/ncomms9079.
[22] V. Nozari, C. Calahoo, L. Longley, T.D. Bennett, L. Wondraczek, Structural integrity, meltability, and variability of thermal properties in the mixed-linker zeolitic imidazolate framework ZIF-62, J. Chem. Phys. 153 (2020), https://doi.org/10.1063/5.0031941.
[23] M.F. Thorne, M.L.R. Gómez, A.M. Bumstead, S. Li, T.D. Bennett, Mechanochemical synthesis of mixed metal, mixed linker, glass-forming metal-organic frameworks, Green Chem. 22 (2020) 2505–2512, https://doi.org/10.1039/d0gc00546k.
[24] A.M. Bumstead, M.L. Ríos Gómez, M.F. Thorne, A.F. Sapnik, L. Longley, J. M. Tuffnell, D.S. Keeble, D.A. Keen, T.D. Bennett, Investigating the melting

behaviour of polymorphic zeolitic imidazolate frameworks, CrystEngComm 22 (2020) 3627–3637, https://doi.org/10.1039/d0ce00408a.
[25] M.F. Thorne, A.F. Sapnik, L.N. McHugh, A.M. Bumstead, C. Castillo-Blas, D. S. Keeble, M. Diaz Lopez, P.A. Chater, D.A. Keen, T.D. Bennett, Glassy behaviour of mechanically amorphised ZIF-62 isomorphs, Chem. Commun. 57 (2021) 9272–9275, https://doi.org/10.1039/d1cc03469c.
[26] L. León-Alcaide, R.S. Christensen, D.A. Keen, J.L. Jordá, I. Brotons-Alcázar, A. Forment-Aliaga, G. Mínguez Espallargas, Meltable, Glass-Forming, Iron Zeolitic Imidazolate Frameworks, J. Am. Chem. Soc. 145 (2023) 11258–11264, https://doi.org/10.1021/jacs.3c01455.
[27] L. León-Alcaide, A. Fernández-Alarcón, J. Calbo, D.A. Keen, G. Mínguez Espallargas, Melt-quenched synthesis of a manganese ZIF glass, Chem. Commun. (2025), https://doi.org/10.1039/d5cc02342d.
[28] W.L. Xue, A. Klein, M. El Skafi, J.B. Weiß, F. Egger, H. Ding, S.K. Vasa, C. Liebscher, M. Zobel, R. Linser, J.C. Tan, S. Henke, Mechanochemical synthesis enables melting, glass formation and glass-ceramic conversion in a cadmium-based zeolitic imidazolate framework, J. Am. Chem. Soc. (2025), https://doi.org/10.1021/jacs.5c02767.
[29] M.A. Ali, J. Ren, T. Zhao, X. Liu, Y. Hua, Y. Yue, J. Qiu, Broad mid-infrared luminescence in a metal-organic framework glass, ACS Omega 4 (2019) 12081–12087, https://doi.org/10.1021/acsomega.9b01559.
[30] R. Li, X. Ren, H. Ma, X. Feng, Z. Lin, X. Li, C. Hu, B. Wang, Nickel-substituted zeolitic imidazolate frameworks for time-resolved alcohol sensing and photocatalysis under visible light, J. Mater. Chem. A Mater. 2 (2014) 5724–5729, https://doi.org/10.1039/c3ta15058e.
[31] D. Karapinar, C.E. Creissen, J.G. Rivera De La Cruz, M.W. Schreiber, M. Fontecave, Electrochemical CO2Reduction to ethanol with copper-based catalysts, ACS Energy Lett. 6 (2021) 694–706, https://doi.org/10.1021/acsenergylett.0c02610.
[32] X. Li, J. You, J. Li, Z. Wang, Y. Zhao, J. Xu, M. Duan, H. Zhang, Progress of copper-based Nanocatalysts in advanced oxidation degraded organic pollutants, ChemCatChem 16 (2024), https://doi.org/10.1002/cctc.202301108.
[33] J. Cao, A. Rinaldi, M. Plodinec, X. Huang, E. Willinger, A. Hammud, S. Hieke, S. Beeg, L. Gregoratti, C. Colbea, R. Schlögl, M. Antonietti, M. Greiner, M. Willinger, In situ observation of oscillatory redox dynamics of copper, Nat. Commun. 11 (2020), https://doi.org/10.1038/s41467-020-17346-7.
[34] X. Huang, T. Jones, A. Fedorov, R. Farra, C. Copéret, R. Schlögl, M.G. Willinger, Phase coexistence and structural dynamics of redox metal catalysts revealed by operando TEM, Adv. Mater. 33 (2021), https://doi.org/10.1002/adma.202101772.
[35] N. Masciocchi, S. Bruni, E. Cariati, F. Cariati, S. Galli, A. Sironi, Extended polymorphism in Copper(II) imidazolate polymers: a spectroscopic and XRPD structural study, 2001, https://doi.org/10.1021/ic010384.
[36] W.-L. Xue, C. Das, J.-B. Weiß, S. Henke, Insights into the mechanochemical glass formation of zeolitic imidazolate frameworks, Angew. Chem. Int. Ed. (2024), https://doi.org/10.1002/anie.202405307.
[37] A. Devdass, K. Talukdar, M. Zeller, R.C. Fortenberry, J.W. Jurss, Exploring different equatorial donors in a series of five-coordinate Cu(II) complexes supported by rigid tetradentate ligands, Polyhedron 212 (2022), https://doi.org/10.1016/j.poly.2021.115558.
[38] D.B. Rorabacher, Electron transfer by copper centers, Chem. Rev. 104 (2004) 651–697, https://doi.org/10.1021/cr020630e.
[39] V. Nozari, O. Smirnova, J.M. Tuffnell, A. Knebel, T.D. Bennett, L. Wondraczek, V. Nozari, O. Smirnova, A. Knebel, L. Wondraczek, O. Schott, J.M. Tuffnell, T. D. Bennett, 2200343 (1 of 7) Low-Temperature Melting and Glass Formation of the Zeolitic Imidazolate Frameworks ZIF-62 and ZIF-76 through Ionic Liquid Incorporation, 2022, https://doi.org/10.1002/admt.202200343.
[40] A.M. Bumstead, M.F. Thorne, A. Sapnik, C. Castillo Blas, G.I. Lampronti, T. D. Bennett, Investigating the chemical sensitivity of melting in zeolitic imidazolate frameworks, Dalton Trans. (2022), https://doi.org/10.1039/D2DT02142K.
[41] J.L. Do, T. Friščić, Mechanochemistry: a force of synthesis, ACS Cent. Sci. 3 (2017) 13–19, https://doi.org/10.1021/acscentsci.6b00277.
[42] S. Tanaka, Mechanochemical synthesis of MOFs, in: Metal-organic frameworks for biomedical applications, Elsevier, 2020, pp. 197–222, https://doi.org/10.1016/B978-0-12-816984-1.00012-3.
[43] B. Ravel, M. Newville, ATHENA, ARTEMIS, HEPHAESTUS: data analysis for X-ray absorption spectroscopy using IFEFFIT, J. Synchrotron Radiat. (2005) 537–541, https://doi.org/10.1107/S0909049505012719.
[44] J.J. Rehr, R.C. Albers, S.L. Zabinsky, High-order multiple-scattering calculations of X-ray-absorption fine structure, Phys. Rev. Lett. 69 (1992).
[45] R. Banerjee, A. Phan, B. Wang, C. Knobler, H. Furukawa, M. O'Keeffe, O.M. Yaghi, High-throughput synthesis of zeolitic imidazolate frameworks and application to CO2 capture, Science (1979) 319 (2008) 939–943, https://doi.org/10.1126/science.1152516.
[46] S. Tetteh, Coordination behavior of Ni2+, Cu2+, and Zn2+ in tetrahedral 1-methylimidazole complexes: a DFT/CSD study, Bioinorg. Chem. Appl. 2018 (2018), https://doi.org/10.1155/2018/3157969.
[47] I. Persson, P. Persson, M. Sandström, A.S. Ullström, Structure of Jahn-teller distorted solvated copper(II) ions in solution, and in solids with apparently regular octahedral coordination geometry, J. Chem. Soc. Dalton Trans. (2002) 1256–1265, https://doi.org/10.1039/b200698g.
[48] A. Qiao, T.D. Bennett, H. Tao, A. Krajnc, G. Mali, C.M. Doherty, A.W. Thornton, J. C. Mauro, G.N. Greaves, Y. Yue, A metal-organic framework with ultrahigh glass-forming ability, Sci. Adv. 4 (2018), https://doi.org/10.1126/sciadv.aao6827.
[49] R.S.K. Madsen, M. Stepniewska, Y. Yang, A. Qiao, W.M.W. Winters, C. Zhou, J. König, J.C. Mauro, Y. Yue, Mixed metal node effect in zeolitic imidazolate frameworks, RSC Adv. 12 (2022) 10815–10824, https://doi.org/10.1039/d2ra00744d.
[50] L. Frentzel-Beyme, P. Kolodzeiski, J.B. Weiß, A. Schneemann, S. Henke, Quantification of gas-accessible microporosity in metal-organic framework glasses, Nat. Commun. 13 (2022), https://doi.org/10.1038/s41467-022-35372-5.
[51] K.C. Kim, T.U. Yoon, Y.S. Bae, Applicability of using CO2 adsorption isotherms to determine BET surface areas of microporous materials, Microporous Mesoporous Mater. 224 (2016) 294–301, https://doi.org/10.1016/j.micromeso.2016.01.003.
[52] Y. Yang, S. Kanchanakungwankul, S. Bhaumik, Q. Ma, S. Ahn, D.G. Truhlar, J. T. Hupp, Bioinspired Cu(II) defect sites in ZIF-8 for selective methane oxidation, J. Am. Chem. Soc. 145 (2023) 22019–22030, https://doi.org/10.1021/jacs.3c06981.
[53] T. Wang, Y. Wang, M. Sun, A. Hanif, H. Wu, Q. Gu, Y.S. Ok, D.C.W. Tsang, J. Li, J. Yu, J. Shang, Thermally treated zeolitic imidazolate framework-8 (ZIF-8) for visible light photocatalytic degradation of gaseous formaldehyde, Chem. Sci. 11 (2020) 6670–6681, https://doi.org/10.1039/d0sc01397h.
[54] J. Koppe, A.J. Pell, Structure determination and refinement of paramagnetic materials by solid-state NMR, ACS Phys. Chem. Au 3 (2023) 419–433, https://doi.org/10.1021/acsphyschemau.3c00019.
[55] Y. Du, R.Z. Chen, J.F. Yao, H.T. Wang, Facile fabrication of porous ZnO by thermal treatment of zeolitic imidazolate framework-8 and its photocatalytic activity, J. Alloys Compd. 551 (2013) 125–130, https://doi.org/10.1016/j.jallcom.2012.10.045.
[56] Q. Liu, Z.X. Low, L. Li, A. Razmjou, K. Wang, J. Yao, H. Wang, ZIF-8/Zn2GeO4 nanorods with an enhanced CO 2 adsorption property in an aqueous medium for photocatalytic synthesis of liquid fuel, J. Mater. Chem. A Mater. 1 (2013) 11563–11569, https://doi.org/10.1039/c3ta12433a.
[57] J. Mor, R.B. Nelliyil, R. Kumar, A. Verma, S.K. Sharma, Compression-induced amorphization of ZIF-62 leading to formation of porous glass: overcoming the limitations of current methods, Chemistry-Methods 5 (2025), https://doi.org/10.1002/cmtd.202500045.
[58] J. Mor, R.B. Nelliyil, R. Kumar, A. Verma, S.K. Sharma, Compression-induced amorphization of ZIF-62 leading to formation of porous glass: overcoming the limitations of current methods, Chemistry-Methods (2025), https://doi.org/10.1002/cmtd.202500045.
[59] A. Manceau, A. Matynia, The nature of Cu bonding to natural organic matter, Geochim. Cosmochim. Acta 74 (2010) 2556–2580, https://doi.org/10.1016/j.gca.2010.01.027.
[60] S.S.-Y. Chui, S.M.-F. Lo, J.P.H. Charmant, A. Guy Orpen, I.D. Williams, A chemically functionalizable nanoporous material $[Cu_3(TMA)_2(H_2O)_3]_n$, Science (1979) 283 (5405) (1999) 1148–1150. https://www.science.org.
[61] A.A.O. Younes, A.M.A. Adam, M.S. Refat, A.S. Al-Wasidi, A.A. Almehizia, M.A. Al-Omar, A.M. Naglah, A.M. Al-Obaid, H.M. Alkahtani, A.J. Obaidullah, M.Y. El-Sayed, K.A. Asla, Synthesis of bivalent Ni(II), Cu(II) and Zn(II) complexes of azodicarbonamide in mixture of methanol and aqueous solvents: spectral characterizations and anti-microbial studies, Crystals (Basel). 13 (2023), https://doi.org/10.3390/cryst13030367.